Electronic Supplementary Material (ESI) for Nanoscale.
This journal is © The Royal Society of Chemistry 2019

Supporting information for:

Electrically transmissive alkyne-anchored monolayers on gold

Lucía Herrer,[a,b] Alejandro González-Orive,[c*] Santiago Marqués-González,[d] Santiago Martín,[a,e] Richard J. Nichols,[f] José Luis Serrano,[a,b] Paul J. Low,[g] Pilar Cea,[a,b,e*]

[a] Departamento de Química Física, Facultad de Ciencias, Universidad de Zaragoza, 50009, Zaragoza, Spain.

[b] Instituto de Nanociencia de Aragón (INA) and Laboratorio de Microscopias Avanzadas (LMA), edificio i+d Campus Río Ebro, Universidad de Zaragoza, C/Mariano Esquillor, s/n, 50018, Zaragoza, Spain.

[c] Technical and Macromolecular Chemistry, University of Paderborn, Warburger Strasse 100, 33098 Paderborn, Germany.

[d] Department of Chemistry, Durham University, South Rd, Durham, DH1 3LE, UK.

[e] Instituto de Ciencias de Materiales de Aragón (ICMA), Universidad de Zaragoza-CSIC, 50009, Zaragoza, Spain.

[f] Department of Chemistry, University of Liverpool, Crown Street, Liverpool, L69 7ZD, United Kingdom.

[g] School of Molecular Sciences, University of Western Australia, 35 Stirling Highway, Crawley, Perth, 6009, Australia.

Corresponding authors:

Alejandro González-Orive (agorive@mail.upb.de)

Pilar Cea (pilarcea@unizar.es)

Table of contents

1. ^{1}H NMR spectrum of compound 1

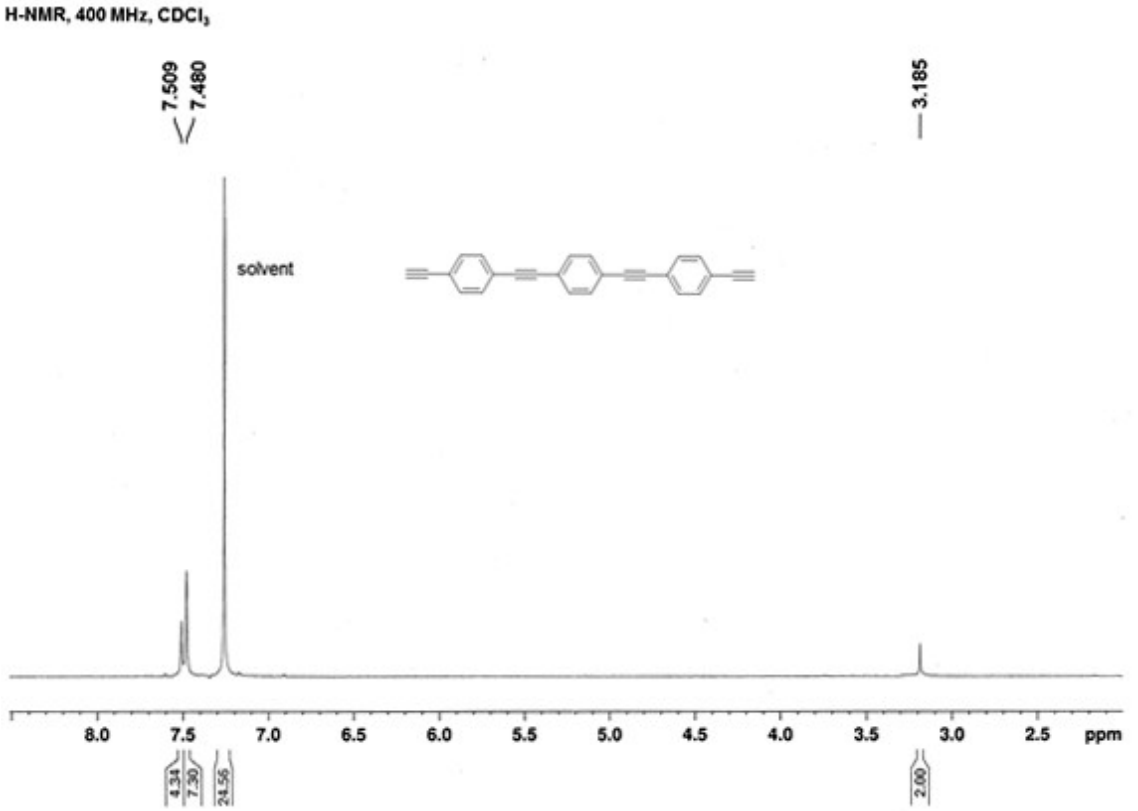

Figure S1. ^{1}H NMR spectrum of compound **1**.

2. Surface coverage for the SAM of 1.

The surface coverage for the SAM of **1** was determined using a quartz crystal microbalance (QCM). The frequency change (Δf) for a QCM quartz resonator before and after the incubation of a gold substrate QCM substrate was recorded. Taking into account the Sauerbrey equation:[1]

$$\Delta f = -\frac{2 \cdot f_0^2 \cdot \Delta m}{A \cdot \rho_q^{1/2} \cdot \mu_q^{1/2}} \qquad \text{(S1)}$$

where f_0 is the fundamental resonant frequency of ca. 5 MHz, Δm is the mass change (g), A is the electrode area, ρ_q is the density of the quartz (2.65 g·cm^{-3}), and μ_q is the shear modulus ($2.95 \cdot 10^{11}$ dyn·cm^{-2}). Figure S2 shows the obtained surface coverage values for the SAM of **1** as a function of the incubation time. As it can be observed the

maximum surface coverage is achieved after ca. 24 hours of incubation. This surface coverage (Γ) has a value of $9.7 \cdot 10^{-10}$ mol·cm^{-2}.

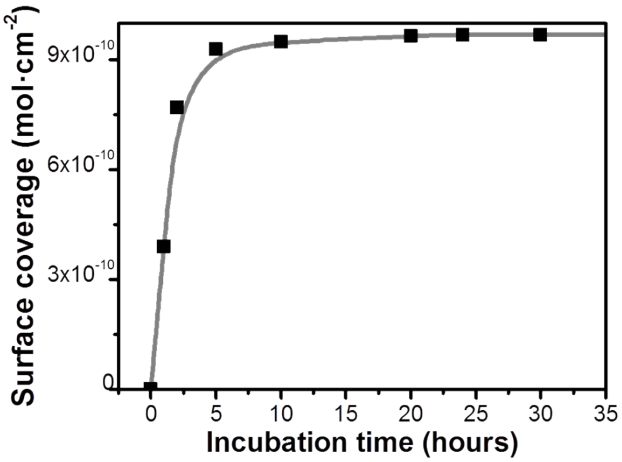

Figure S2. Surface coverage for the SAM of **1** as a function of the incubation time.

3. AFM images for the SAM of 1 after 24 h incubation.

AFM images for the SAM of **1** were obtained and a representative one is shown in Figure S3. The thickness of the SAM was determined by scratching the film with the AFM tip (Figure S3.b). A cross-section profile (Figure S3.c) and the depth profile histogram (Figure S3.d) provide a film thickness of ca. 1.7 nm.

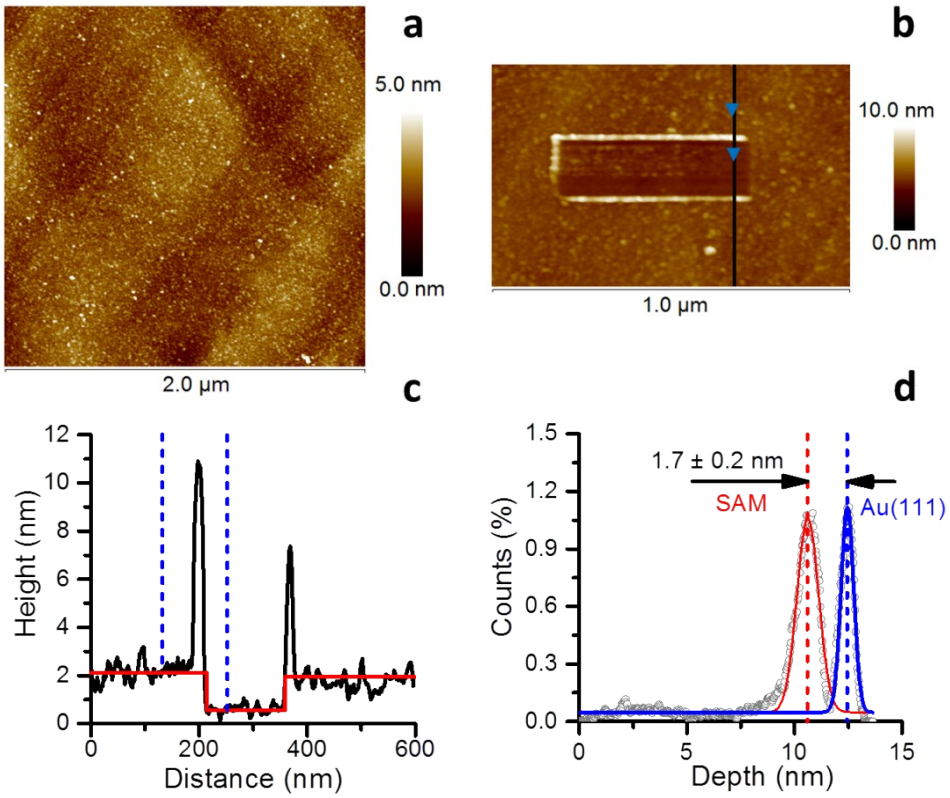

Figure S3. **(a)** 2.0 x 2.0 µm^2 AFM image showing the topography of a SAM of **1** on an Au(111) surface. **(b)** AFM image of a 500 x 125 nm^2 scratch made in a smooth Au(111) terrace covered by the SAM of **1**, and **(c)** representative cross-section profile across the scratch. **(d)** Depth profile histogram exhibiting the depth value distributions related to bare gold, blue line, and the SAM, red. From the height difference between the later, the thickness of the SAM of **1**, i.e. 1.7 nm, can be obtained.

4. Determination of the thickness of the SAM of 1 by XPS.

The film thickness was also determined by evaluating the gold Au-4f signal attenuation in XPS core-level spectra recorded before and after the deposition of the SAM (Figure S4). The thickness estimated by this method is in excellent agreement with the one calculated from AFM images.

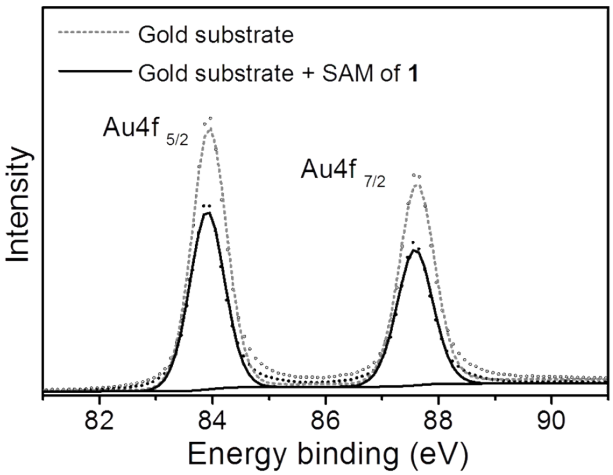

Figure S4. XPS spectra of Au-4f photoelectrons of a gold substrate and a gold substrate covered by a SAM of **1**.

5. Raman spectrum of the powder of 1 and SERS spectrum of the SAM of 1.

Figure S5 shows the Raman spectrum of the powder of **1**. The main bands in this spectrum can be assigned to:[2]

- Band at 500 cm^{-1}: out-of-plane ring deformation vibration of 1,4-disubstituted benzenes (520-445 cm^{-1}).
- Band at 776 cm^{-1}: aromatic out-of-plane C-H deformation vibrations and ring out-of-plane vibrations; para-disubstituted benzenes absorb strongly at 860-780 cm^{-1}.
- Bands at 1124 and 1180 cm^{-1}: aromatic in-plane C-H deformation vibrations which occur in the region 1290-990 cm^{-1}.
- Band at 1592 cm^{-1}: aromatic C= C stretching vibrations.
- Band at 2104 cm^{-1}: alkyne C≡C stretching vibrations. Monosubstituted alkynes, -C ≡ CH (2100-2150 cm^{-1}).
- Band at 2208 cm^{-1}: disubstituted alkynes -C ≡ C- (2260-2190 cm^{-1}).

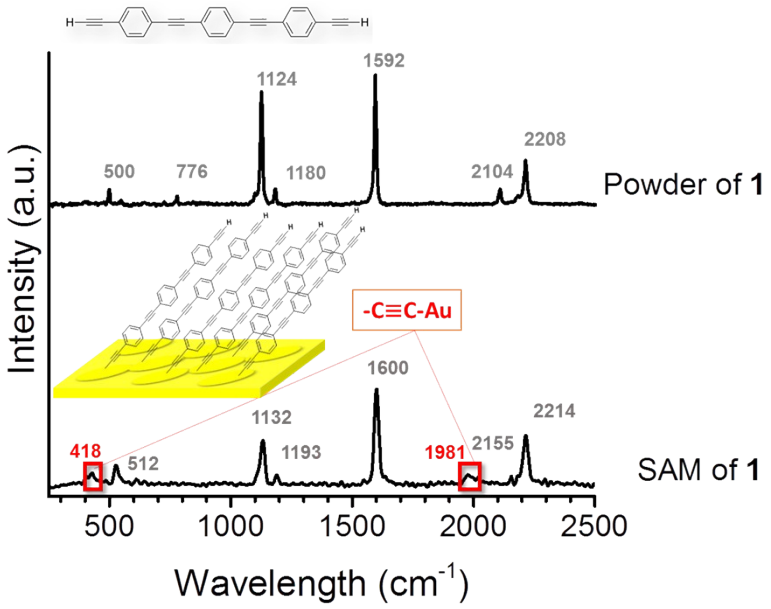

Figure S5. Raman and SERS spectra of the powder of **1** and a SAM of **1**, respectively.

Importantly, the SERS spectrum of the SAM of **1** shows the appearance of two new bands at 418 and 1981 cm^{-1} which have been previously attributed to the formation of a -C≡C-Au bond.

6. Molecular organization of 1 within the SAM studied by STM.

Further studies of the molecular organization in the SAM are important to get a full picture of the properties of the SAM of **1**, including specifically the electrical behavior described in this contribution. Thus, to better understand the nature of the SAMs of **1**, high-resolution scanning tunneling microscopy (STM) was used to study the growth of the film at early and late incubation times in the self-assembly process. Figure S6.a and Figure S6.b show the STM images obtained for a SAM of **1** prepared onto Au(111) surfaces after incubation times, t_i, of 1 h and 24 h, respectively.

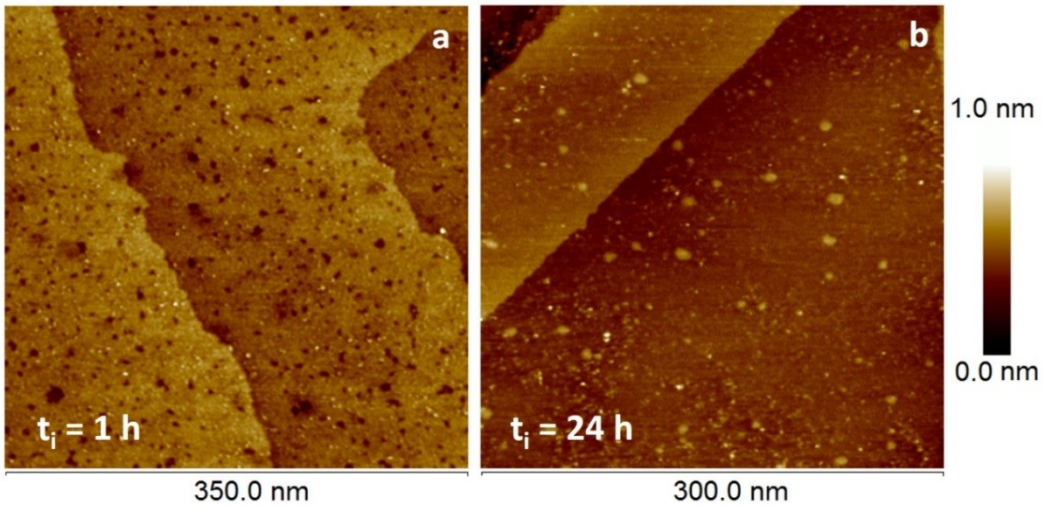

Figure S6. STM images of a SAM of **1** for: **(a)** incubation of a gold substrate into a $1 \cdot 10^{-4}$ M solution of **1** in $CHCl_3$ for 1 hour and **(b)** after 24 hours of incubation.

To fully understand the results and information provided by these STM images we describe first the well-known and widely studied alkyl- and aryl-thiol assemblies in SAMs that can be taken as reference model systems; in fact, a number of recent contributions have shown that both aliphatic and aromatic ethynyl-terminated molecules give rise to SAMs on Au(111) surfaces which are very similar to those exhibited by analogous thiol-terminated molecules in terms of surface coverage and electrochemical behavior.[3-5] Some ethynyl-terminated molecules (both alkyl- and aryl-based moieties) have been recently reported to form self-assembled monolayers (SAMs) on Au(111) and also on other single-crystalline metal surfaces such as Pd(111), Pt(111), Rh(111), and Ir(111) analogous to those exhibited by organic thiols.[3, 4, 6] Typically, the exposure of pristine gold substrates to alkanethiol solutions, when both the concentrations and deposition times are properly optimized, results in densely packed monolayers with the molecules slightly tilted versus the surface normal (~30º). It is well-known that upon the formation of the SAM, the Au(111) surface undergoes structural alterations such as lifting of the herringbone reconstruction, formation of vacancy islands (etched pits), and the production of gold adatoms which can, under certain circumstances, provide energetically favored adsorption sites.[7, 8] On such a reconstructed surface an alkanethiol molecule occupies a surface adsorption site confined by three gold atoms (namely fcc hollow, hcp hollow, bridge or on top adsorption sites), whilst lateral van der Waals interactions between neighboring alkyl chains of the adsorbed molecules are maximized. The fractional surface coverage (Θ) is defined as the quotient between the

number of adsorption sites occupied by molecules and the number of adsorption sites available (gold atoms). Simple alkanethiols result in a molecular fractional surface coverage of Θ = 1/3 (0.33), with nearest neighbor sulfur-sulfur distances of ~0.5 nm, as determined by XPS, STM, and electrochemical measurements.[9-11] Subsequently, if 1 cm^2 of Au(111) is occupied by $1.4 \cdot 10^{15}$ gold atoms, then a gold surface density of $2.32 \cdot 10^{-9}$ $mol \cdot cm^{-2}$ is obtained. For the maximum saturated (√3 x √3)-R30° lattice and c(4 x 2) superlattice (unit cell of the adsorption sites), a fractional surface coverage of Θ = 0.33 (i.e. one molecule out of each three gold atoms) results in a maximum molecule surface coverage of $7.75 \cdot 10^{-10}$ $mol \cdot cm^{-2}$.[12] Different surface coverages are possible depending on the molecular concentration, incubation time, structure and nature of the bridging molecule, distal functional groups, etc.[9, 13] In particular, for aromatic thiols slightly lower values of fractional surface coverage have been reported in comparison to those of alkyl thiols,[9, 13, 14] although by increasing the number of phenyl units in the molecule backbone, both the structural order and the surface coverage are noticeably increased.[15]

Turning back to the SAMs of compound **1**, at relatively early stages of formation of the SAM (e.g, t_i = 1 h) numerous vacancies or pits distributed over the sample surface are observed (Figures S6.a and S7.a), which are only observed for short immersion times, namely t_i = 1 h and cannot be detected for long immersion times, t_i = 24 h. Some small two dimensional adatom islands (bright spots) can be also detected in the image of films incubated for 1 h. A representative cross section of a STM image showing 0.24 nm step heights corresponding to pits is depicted in Figure S7.b. These pits exhibit an average width of 5.4 ± 1.5 nm (Figure S7.c).

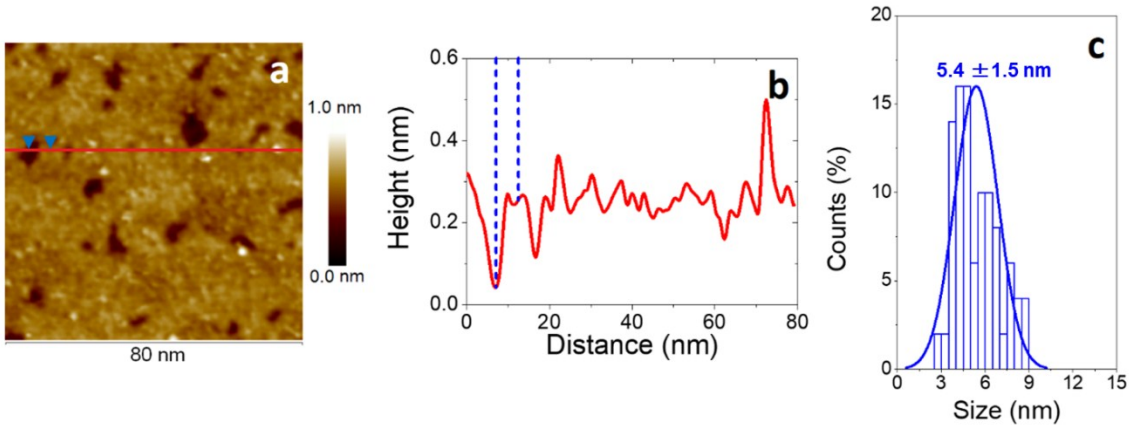

Figure S7. **(a)** 80 x 80 nm^2 STM image showing the presence of homogeneously distributed pits/vacancies for a SAM of **1** incubated for 1 h on Au (111). **(b)** Representative cross-section of

(a) through the red line showing size and height of pits/vacancies and small gold adatom islands. **(c)** Histogram showing the distribution of pit width data values.

From STM images of SAMs of **1** incubated for t_i = 1 h, a fractional surface coverage, $\Theta_{PIT,}$ of 0.12 has been estimated, Figure S8, i.e. 12 % of the gold surface area corresponds to vacancies/pits.

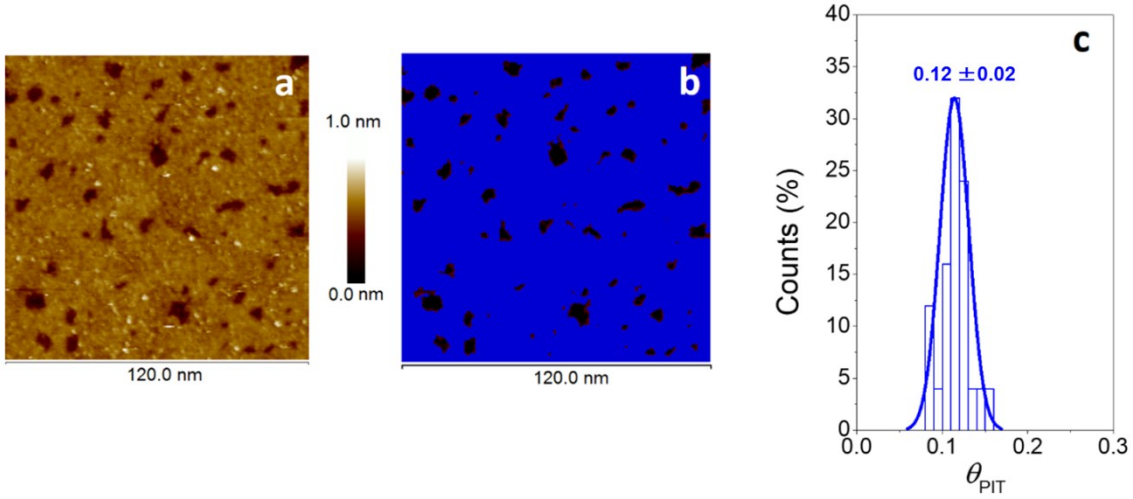

Figure S8. **(a)** 120 x 120 nm^2 STM images showing the presence of homogeneously distributed pits/vacancies in the SAM of **1** on Au (111) for an incubation time of 1 hour. **(b)** Blue-mask in (a) unveils regions, dark-brown areas, exhibiting heights below the selected threshold. **(c)** Histograms showing the distribution of surface coverage data values.

The STM images obtained for t_i = 1 h also exhibit regions where not only pits/vacancies but also gold islands are present (Figure S9), together with some isolated areas exhibiting short-range molecular ordering of the growing monolayer (no long-range ordering is detected). By carrying out cross section profiles of the STM images (Figure S9.a and b), the width of the pits and the arising gold adatom islands has been statistically determined. Interestingly, the average width of the pits increased from 5.4 nm (Figure S7.c) to 12.6 nm (Figure S9.d) whilst the newly formed gold adatom islands are 7.2 nm wide (Figure S9.c).

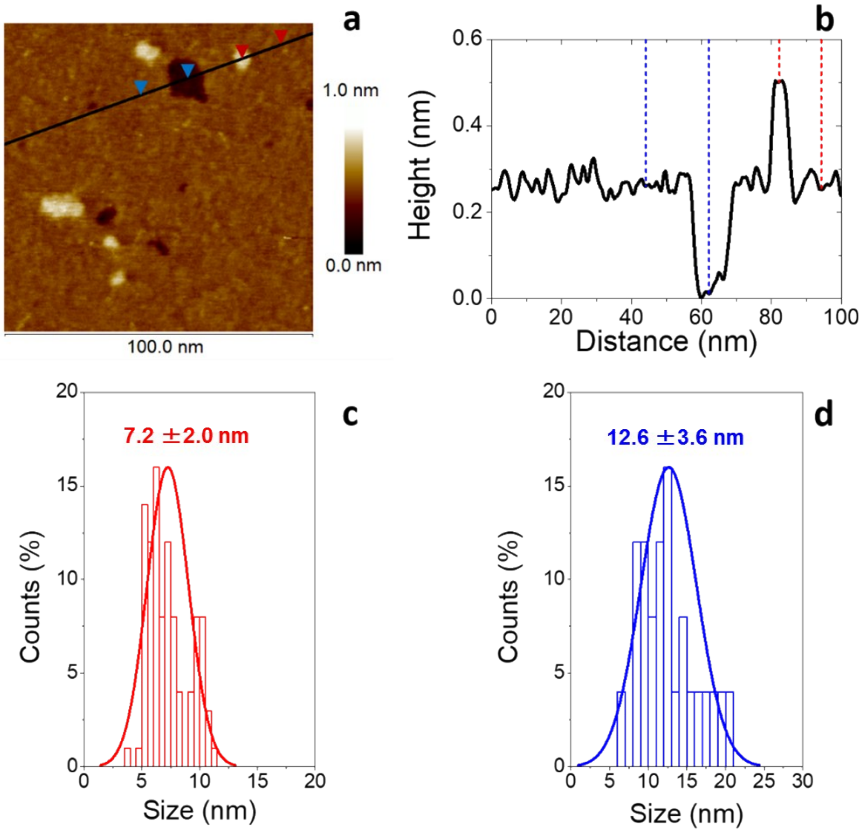

Figure S9. **(a)** 100 x 100 nm^2 STM image showing the topography of a SAM of **1** on an Au(111) surface. **(b)** Representative cross section through the black line in (a) made in a smooth Au(111) terrace covered by the SAM of **1**, showing width of pits and gold adatom islands. **(c)** and **(d)** Histograms showing the gold adatom island (red) and pit (blue) width data values, respectively.

High-resolution STM images obtained for the SAM of **1** for t_i = 1 h are depicted in Figure S10, where parallel rows of molecules are clearly observable, exhibiting a molecular periodicity in the order of 1.1 nm. Comparable inter-row distances of 1.2 nm were reported by Matisons *et al.*[4] for ethynylbenzene SAMs prepared on gold from dichloromethane solutions. Also similar results have been obtained by Buck and co-workers[16] for biphenylthiol SAMs at low incubation times, which arranged into an incommensurate (2√3 x 2√3) lattice. Thus, the surface coverage of vacancies for t_i = 1 h, i.e. Θ_{PIT} = 0.12, along with the gold adatoms coming from the lifting of the herringbone reconstruction, i.e., Θ = 0.045,[14] results in an adatom surface coverage of Θ_{ad} = 0.165. Interestingly, this value of the adatom surface coverage is nearly half as much as is required to satisfy the gold adatom requirements for a 1:1 RC≡C-Au

complex in a densely packed SAM of **1** on Au(111) (Θ = 0.33, i.e. the fractional surface coverage corresponding to a commensurate lattice). Consequently, a SAM of **1** with a stoichiometry of a RC≡C-Au_{adatom}-C≡CR complex (i.e. *two* RC≡C- adsorbates per gold adatom) might explain the early stages of the monolayer formation, assuming that the surface density of pits is related to the gold atoms lifted from the surface, which are subsequently available to form adatom constructions.

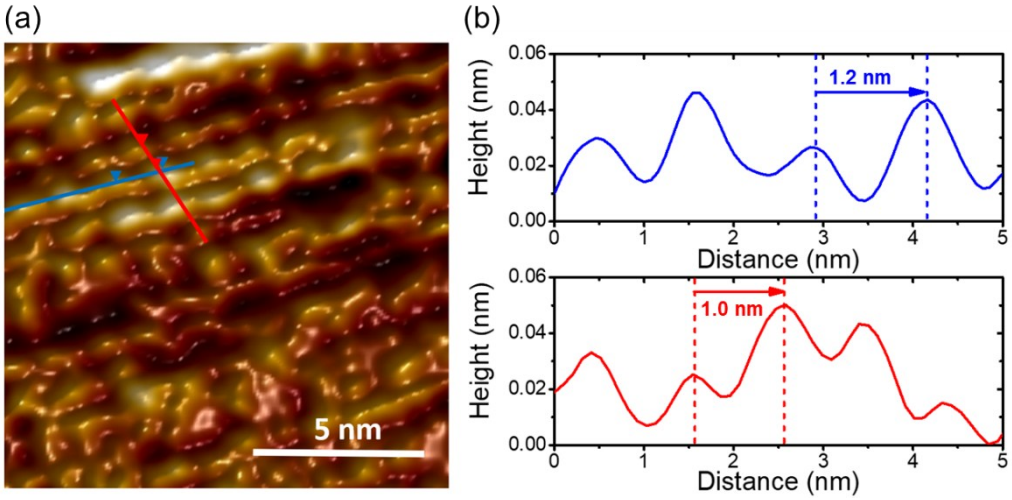

Figure S10. **(a)** 13 x 13 nm^2 STM images showing the presence of ordered and disordered regions in a SAM of **1** on Au (111) for an incubation time of 1 hour. **(b)** Representative cross-sections of (a) through the red and blue line showing molecular periodicity.

Finally, it is also worth of note that when the incubation time is increased to 24 h, the SAM of **1** is much more homogeneous, and pits/vacancies are no longer detected (Figure S6.b). On the contrary, gold islands, with a single atom height, are observed decorating the triangular-shaped terraces of Au(111). A representative cross section of a STM image showing 0.24 nm step heights corresponding to gold adatom islands is depicted in Figure S11. No pits are detected for large immersion times, namely t_i = 24 h. An average width of 8.0 ± 2.1 nm (after subtraction of the tip convolution) can be estimated for gold adatom islands.

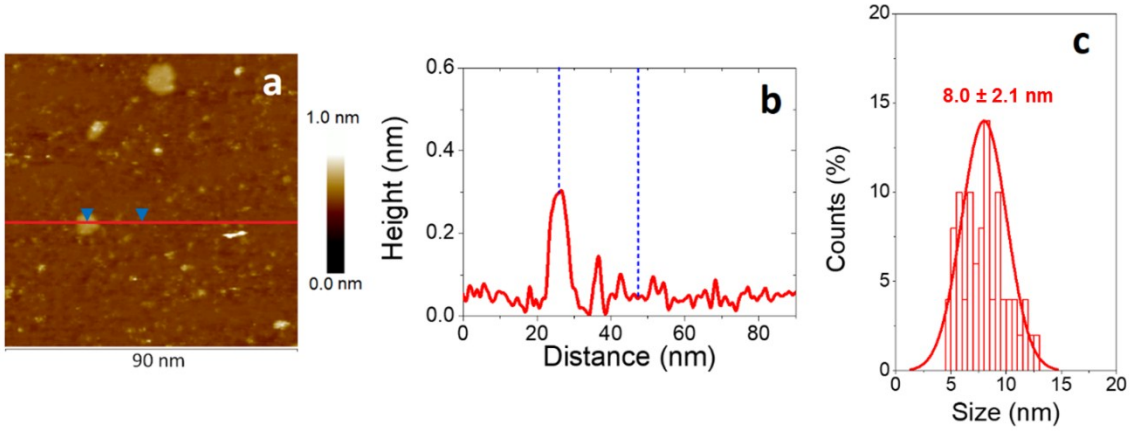

Figure S11. **(a)** 90 x 90 nm^2 STM images showing the presence of homogeneously distributed gold adatom islands in a SAM of **1** on Au (111) for t_i = 24 h. **(b)** Representative cross-section of (a) through the red line showing size and height of gold adatom islands. **(c)** Histogram showing the distribution of gold adatom island width data values.

Therefore, the RC≡C-Au$_{adatom}$-C≡CR structures associated with short times of incubation may be part of the chemistry of activation of the molecule and the growth process of the monolayer. As the film grows (between t_i =1 and t_i = 24 h) the adatoms are expelled to give the gold islands/single atom height plateaus, and the molecules get packed into a denser, well ordered film. This behavior, namely the occurrence of pits/vacancies for short incubation times and their progressive replacement by gold islands for longer immersion times, has also been reported for aromatic-based thiol SAMs on Au(111)[16] and is related to a significant increase in the surface coverage and decrease in the area per molecule. Indeed, these authors showed for SAMs of 4-methyl-4´-mercaptobiphenyl on Au(111) ordered domains alternated by depressions exhibiting a depth of 2.4 Å, i.e. pits, with relatively high values of molecule area. However, for longer immersion times, monoatomic high gold islands along with a higher molecule surface coverage, exhibiting ordered phases arranged in a (2√3 x √3)R30° and (√3 x √3)R30° unit cells and an area per molecule of 21.6 Å^2, were obtained.[17] Most importantly, the latter commensurate lattices have also been obtained for SAMs of OPE-based thiol molecules, i.e. arenethiols with three phenyl rings, on gold, for high coverage specimens (long incubation times).[18-20] Matei *et al.*[21] found a tightly packed hexagonal (2 x 2) lattice exhibiting an area per molecule of 28.7 Å^2 for the result of the self-assembly of 1,1´-biphenyl-4-thiol on Au(111). For long immersion times, gold terraces appeared decorated with gold islands exhibiting irregular shapes and sizes

below 20 nm. The nucleation of gold islands has been related to the formation of RS-Au adatom complexes.[9] Additionally, SAMs exhibiting σ Au-C≡N-R bonds from isocyanide-terminated OPE-based molecules have also been reported to form densely packed SAMs on Au(111) and Pd(111) substrates.[22] In both cases, a tilt angle of ~24° was reported. Crudden *et al.*[23] described the formation of carbene-based SAMs on Au(111) exhibiting the formation of pits/vacancies and structures stable and compact enough as not to allow for alkanethiol incorporation/ replacement. Finally, as previously stated, Matisons *et al.*[4] also reported condensed and highly tilted SAMs of ethynylbenzene (~41° measured by ellipsometry).

As previously stated, the SAM of **1** onto pristine Au(111) surfaces is basically determined by the balance between the R-C≡C-Au surface interaction and the van der Waals interactions occurring between the tail phenyl rings. In this regard, Jiang *et al.*[24] have proposed two different R-C≡C-Au_{adatom}-C≡C-R staple motifs for ethynyl-terminated phenyl-based molecules depending on both the nature of the bonds established with the surrounding gold atoms and the packing density as well. The authors provided reliable evidences obtained by DFT for the formation of R-Ph-C≡C-Au_{adatom}-C≡C-Ph-R complexes when gold adatoms are available in the Au(111) surface. The latter staple adatom moieties would be energetically favored in comparison with the R-Ph-C≡C- motifs adsorbed at fcc hollow sites. These structures are similar to the thoroughly reported RS-Au_{adatom}-SR complexes for organic thiol SAMs on gold surfaces. However, by applying first principles molecular dynamics (MD), an additional stabilizing effect due to the π-bonding of the C≡C to the gold atoms immediately below could be established for the R-C≡C-Au_{adatom}-C≡C-R complex, giving rise then to what has been called the π-staple motif. Therefore, the latter new π-staple structure would adopt a more lying-down configuration than the σ-stapled one which would exhibit a more vertical but still tilted structure. Thus, according to the authors, at low coverages, the **1** molecules would chemisorb onto the Au(111) surface by mainly adopting this π-staple R-C≡C-Au_{adatom}-C≡C-R complex. On the other hand, at higher coverages, the increasing van der Waals interactions between the tail phenyl rings of **1** molecules should overcome this additional π-C≡C-Au bonding, favoring then the σ-staple motif and decreasing thus the tilt angle with respect to the surface normal. Consequently, the latter would be energetically favored for high incubation times**,** namely t_i = 24 h. Accordingly, the thicknesses that have been obtained by means of AFM scratching of

the **1** molecule layer, i.e. 1.2 nm for t_i = 1 h (Figure S12), and 1.7 nm for t_i = 24 h (Figure S3), would be in very good agreement with an evolution from an initial lying-down π-staple motif to the final standing-up σ-R-C≡C-Au_{adatom}-C≡C-R complex, as elegantly predicted by Jiang *et al*.[24] Most importantly, both the σ and π Au_{adatom}-C≡C-R covalent bondings would provide a strong electronic coupling because of an uninterrupted conjugation (π-delocalized electrons) between the gold electrode and the chemisorbed **1** molecules.

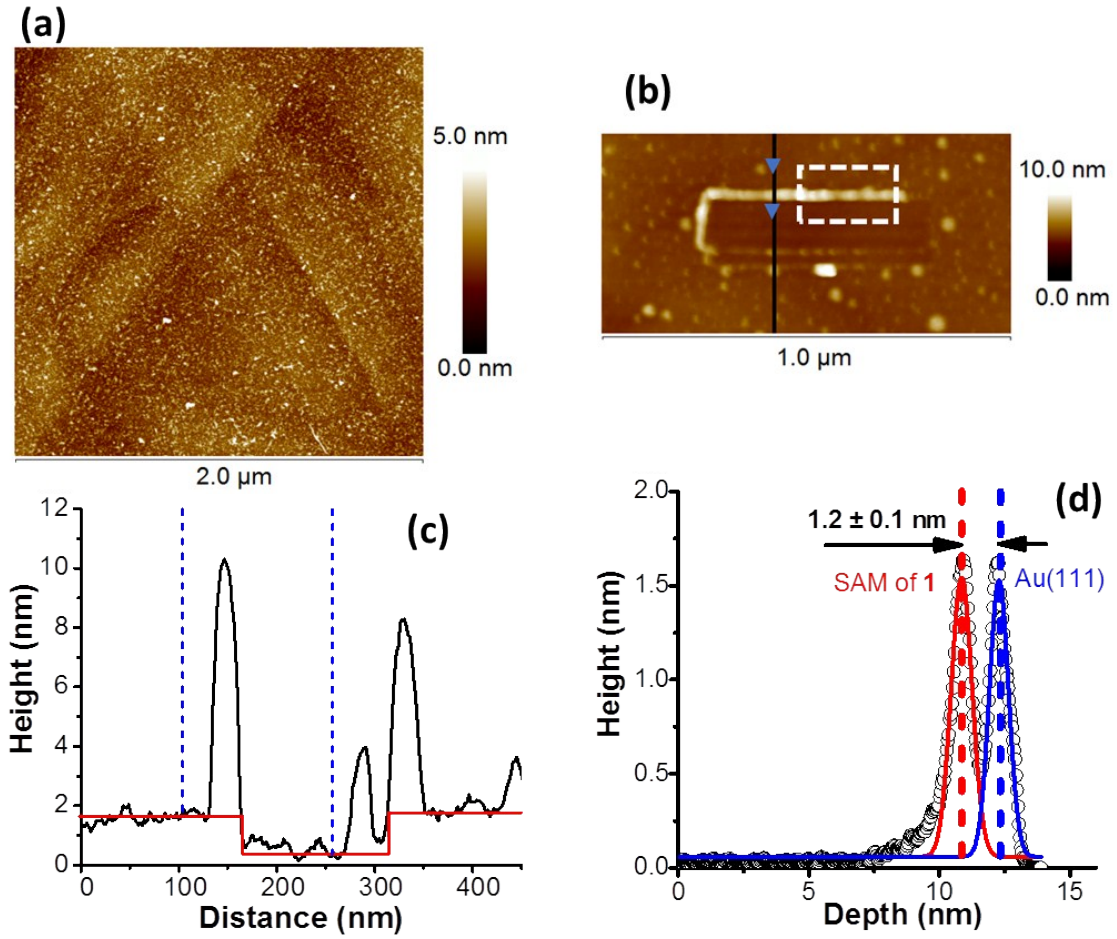

Figure S12. **(a)** 2.0 x 2.0 µm² AFM image showing the topography of a SAM of **1** on an Au(111) surface incubated for 1 hour. **(b)** AFM image of a 500 x 125 nm² scratch made in a smooth Au(111) terrace covered by the SAM of **1**, and **(c)** representative cross-section profile across the scratch. **(d)** Depth profile histogram exhibiting the depth value distributions related to bare gold, blue line, and the SAM, red. From the height difference between the later, the thickness of the SAM of **1**, i.e. 1.7 nm, can be obtained.

The proposed structures, i.e. σ-staple R-C≡C-Au_{adatom} complexes as well as gold adatom islands, would justify the high tilt angle observed for the SAM of **1** by AFM and

XPS measurements, and, together with the QCM and contact angle results, would also account for a noticeable coverage of the Au(111) surface.

7. Capacitance of the SAM of 1 upon cycling.

500 consecutive cyclic voltammograms of the SAM of **1** at high scan rates (1 $V \cdot s^{-1}$) in the window potential from -0.1 V to -0.6 V in 0.5 M KCl were obtained to verify the stability of the film. As shown in Figure S13 the voltammograms remain practically unaltered upon cycling.

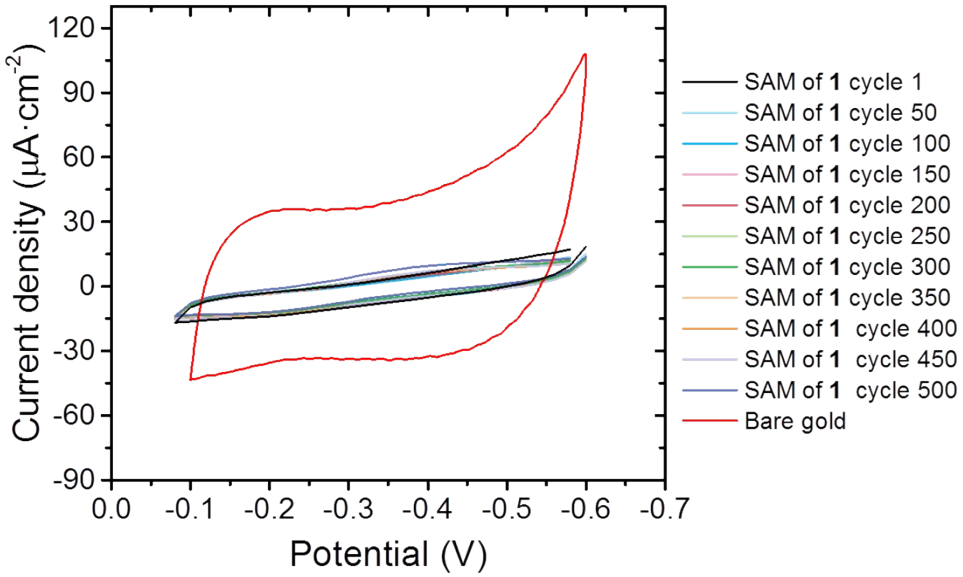

Figure S13. Cyclic voltammograms of a bare gold electrode and the SAM of **1** in a 0.5 M KCl aqueous solution recorded at a scan rate of 1 V·s-1. For the SAM of **1** the number of cycles after which the voltammogram was recorded is indicated in the figure legend.

8. Functionalization of the SAM of 1 with gold nanoparticles.

A dispersion of naked gold nanoparticles (AuNPs) was prepared by adding rapidly drop by drop 0.5 mL of a $1.0 \cdot 10^{-3}$ M $NaBH_4$ aqueous solution to 30 mL of a $1.0 \cdot 10^{-5}$ M $HAuCl_4$ aqueous solution with vigorous stirring into an ice-water bath. The hydrodynamic diameter of these AuNPs was found to be ~8 nm, as determined by Dynamic Light Scattering (DLS, % number). Incubation of the SAMs in the dispersion

of AuNPs takes place 15 min after the mixture of the reactants. The SAMs were incubated for ca. 3 hours into the AuNPs dispersion to form the gold substrate/SAM/AuNPs devices. Afterwards, the substrate was thoroughly rinsed with water and dried with a nitrogen stream. The deposition process and the required incubation time were determined by means of QCM, Figure S14.

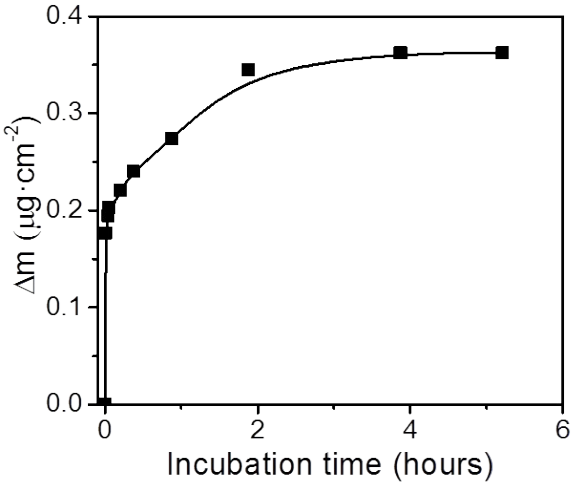

Figure S14. Deposition of gold nanoparticles vs. the incubation time.

9. Electroreduction of the SAM of 1.

Figure S15 shows the voltammograms registered for the SAM of **1** on Au(111) in 0.1 M NaOH. A large cathodic peak attributable to the one-electron desorption of **1** molecules, blue voltammogram, located at -1.25 V (vs. Ag/AgCl) and labelled as C1 peak, preceding *HER* (hydrogen evolution reaction), can be easily identified, in contrast to the featureless voltammogram exhibited by the bare Au(111) electrode (voltammogram in red). However, the value of faradaic charge associated with C1 is significantly higher than that proceeding exclusively from the one-electron electrochemical desorption of **1** (~maximum of -0.08 $mC \cdot cm^{-2}$).[15] Consequently, C1 necessarily must include other faradaic process(es).

Interestingly, in the seminal contribution by Muglali and co-workers a large faradaic charge was also observed for (apparently) the desorption of an organic film.[25] The occurrence of three processes was used to explain such a large faradaic charge (1.32 $mC \cdot cm^{-2}$): (i) the electrodesorption of the organic film, (ii) the HER, and (iii) the catalyzed HER. Thus, a detailed mechanism for *HER* kinetics enhancement when (4-(4-

(4-pyridyl)phenyl)phenyl)methanethiol (PyPP1) molecules are electrochemically desorbed from an Au(111) electrode was proposed by these authors, who demonstrated that after desorption, the PyPP1 layer was suspended in the interface plane with its two dimensional (2D) ordered structure preserved. The HER catalysis was attributed to an optimum orientation of water molecules (to favor *HER*).[25, 26] Such a preferential orientation of the water molecules was attributed to the presence of hydrated Na^+ ions in the interface defined by the negatively polarized Au surface and the negatively charged assembled thiolate layer (still preserving the 2D order) after desorption. Similarly, the faradaic charge obtained for the SAM of **1** from peak C1 (Figure S12) is -1.23 $mC \cdot cm^{-2}$, which is in very good agreement with the above-mentioned observations for the SAM of PyPP1. Interestingly, this *HER* catalytic effect, to the best of our knowledge, has not been reported in the case of alkyne molecules.

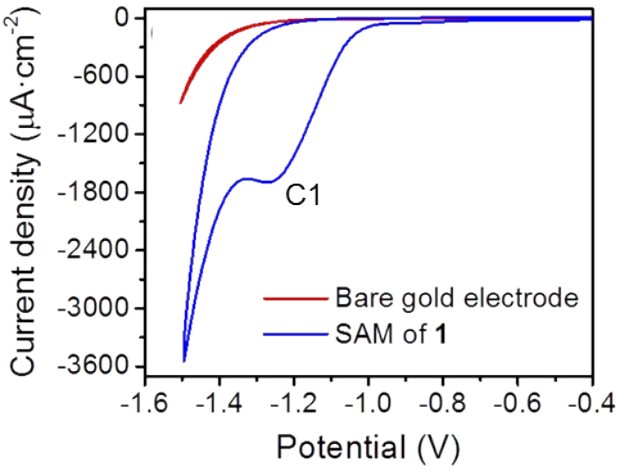

Figure S15. Cyclic voltammograms for the indicated electrodes recorded in aqueous 0.1 M NaOH at 0.05 $V \cdot s^{-1}$ vs Ag/AgCl.

10. Calibration and *I-V* curves registered for the SAM of 1 by using the "STM touch-to-contact" method.

In the "STM touch-to-contact" method, the STM tip is positioned just in contact with the upper surface of the SAM. Both penetration of the STM tip into the film and any significant gap between the STM tip and the monolayer are avoided. In order to achieve this an independent and precise determination of the SAM thickness is required as well as a calibration of the initial tip–substrate separation. A quantification of the current decay as expressed by ($d\ln I/ds$) is required for the tip-substrate distance

calibration as has been reported previously.[27] The collected ln$I$ vs. s data was plotted the (Figure S16.b), taking care to omit the non-linear region at the beginning of the ln$I$ vs s curve. This non-linear region was attributed to an initial inertia in the retraction process caused by a piezo delay. Values of d ln$I$/ds obtained here were typically in the range of 6.96 ± 1.01 nm^{-1} as determined from 23 $I(s)$ traces which featured a monotonic exponential decay of the tunneling current (Figure S16.a). This (d ln$I$/ds) value was then used in conjunction with an extrapolation to the conductance value corresponding to the point at which the gold STM tip contacts the gold substrate (taken as G_0 where G_0 = $2e^2/h$ = 77.5 μS). With these values equation S2 allows an estimation of the voltage and current set-point values where the STM tip would touch the top of the SAM.

$$s_0 = \frac{ln\left(G_0 U_t / I_0\right)}{dln(I)/ds} \quad \text{(S2)}$$

By using as set point parameters U_t = 0.6 V (tip bias) and I_0 = 0.33 nA (set point current) together with equation S2 a tip-substrate distance of 1.7 nm (s) was obtained. This tip-surface separation is in agreement with the monolayer thickness. This indicates that when these parameters are used the STM is positioned just touching the SAM in the so-called "touch-to-contact" configuration. Under these conditions, more than 400 I-V curves for a SAM of **1** were recorded (Figure S16.c).

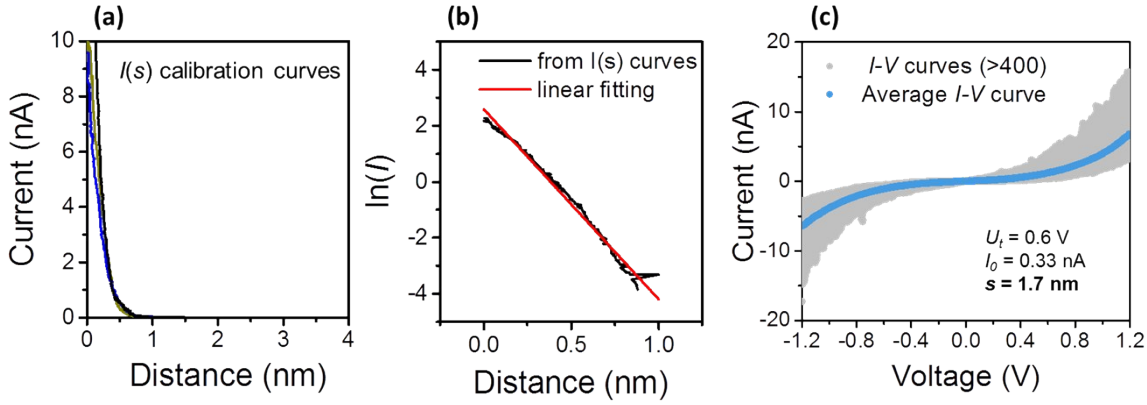

Figure S16. a) Examples of $I(s)$ calibration curves registered. **b)** ln I vs s plots used for the calibration of tip–substrate distance starting from the $I(s)$ calibration curves. Just the linear section for each $I(s)$ curve is used. Red line shows the linear fitting. **c)** I-V curves registered at 1.7 nm tip-substrate distance after tip-substrate distance calibration.

11. Comparison of V_{trans} values for 1 and other molecular wires.

Table S1. V_{trans} values determined in the indicated reference for the molecules in the first column.

Molecule	V_{trans} (V)	Reference
	0.51	This work
	0.64	28
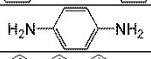	0.59	28
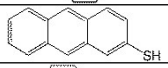	0.60	29
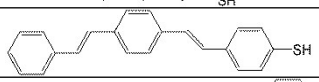	0.57	29
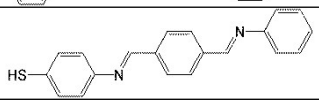	0.85	30
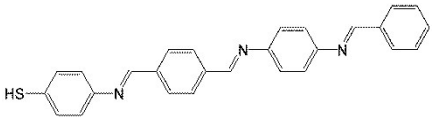	0.75	30

12. References.

1. G. Sauerbrey, Z. Physik, 1959, **155**, 206.
2. G. Socrates, *Infrared and Raman characteristic group frequencies: tables and charts. 3rd Edition.*, (Wiley., 2004).
3. H. J. Yoon, C. M. Bowers, M. Baghbanzadeh, G. M. Whitesides, J. Am. Chem. Soc., 2014, **136**, 16.
4. A. M. McDonagh, H. M. Zareie, M. J. Ford, C. S. Barton, M. Ginic-Markovic, J. G. Matisons, J. Am. Chem. Soc., 2007, **129**, 3533.
5. D. Z. Manrique, C. Huang, M. Baghernejad, X. Zhao, O. A. Al-Owaedi, H. Sadeghi, V. Kaliginedi, W. Hong, M. Gulcur, T. Wandlowski, M. R. Bryce, C. J. Lambert, Nat. Commun., 2015, **6**, 6389.
6. Y. Fu, S. Chen, A. Kuzume, A. Rudnev, C. Huang, V. Kaliginedi, M. Baghernejad, Q. J. Hong, T. Wandlowski, S. Decurtins, S.-X. Liu, Nat Commun, 2015, **6**, 6403.
7. P. Carro, X. Torrelles, R. C. Salvarezza, Phys. Chem. Chem. Phys., 2014, **16**, 19017.
8. Y. Wang, Q. Chi, N. S. Hush, R. Reimers, J. Zhang, J. Ulstrup, J. Phys. Chem. C., 2011, **115**, 10630.
9. C. Vericat, M. E. Vela, G. Benitez, P. Carro, R. C. Salvarezza, Chem. Soc. Rev., 2010, **39**, 1805.
10. J. C. Love, L. A. Estroff, J. K. Kriebel, R. G. Nuzzo, G. M. Whitesides, Chem. Rev., 2005, **105**, 1103.
11. T. Burgi, Nanoscale, 2015, **7**, 15553.
12. A. H. Suroviec, Chem. Educator, 2012, **17**, 83.
13. E. Pensa, P. Carro, A. A. Rubert, G. Benítez, C. Vericat, R. C. Salvarezza, Langmuir, 2010, **26**, 17068.
14. M. C. R. González, A. G. Orive, P. Carro, R. C. Salvarezza, A. H. Creus, J. Phys. Chem. C, 2014, **118**, 30013.

15. R. C. Salvarezza, P. Carro, J. Electroanal. Chem., 2018, **819**, 234.
16. W. Azzam, C. Fuxen, A. Birkner, H.-T. Rong, M. Buck, C. Wöll, Langmuir, 2003, **19**, 4958.
17. P. Angelova, H. Vieker, N. E. Weber, D. Matei, O. Reimer, I. Meier, S. Kurasch, J. Biskupek, D. Lorbach, K. Wunderlich, L. Chen, A. Terfort, M. Klapper, K. Mullen, U. Kaiser, A. Golzhauser, A. Turchanin, ACS Nano, 2013, **7**, 6489.
18. A. Dhirani, R. W. Zehner, R. P. Hsung, P. Guyot-Sionnest, L. R. Sita, J. Am. Chem. Soc., 1996, **118**, 3319.
19. G. H. Yang, Y. L. Qian, C. Engtrakul, L. R. Sita, G. Y. Liu, J. Phys. Chem. B, 2000, **104**, 9059.
20. J. J. Stapleton, P. Harder, T. A. Daniel, M. D. Reinard, Y. Yao, D. W. Price, J. M. Tour, D. L. Allara, Langmuir, 2003, **19**, 8245.
21. D. G. Matei, H. Muzik, A. Golzhauser, A. Turchanin, Langmuir, 2012, **28**, 13905.
22. J. J. Stapleton, T. A. Daniel, S. Uppili, O. M. Cabarcos, J. Naciri, R. Shashidhar, D. L. Allara, Langmuir, 2005, **21**, 11061.
23. C. M. Crudden, J. H. Horton, I. I. Ebralidze, O. V. Zenkina, A. B. McLean, B. Drevniok, Z. She, H.-B. Kraatz, N. J. Mosey, T. Seki, E. C. Keske, J. D. Leake, A. Rousina-Webb, G. Wu, Nat. Chem., 2014, **6**, 409.
24. Q. Tang, D.-e. Jiang, J. Phys. Chem. C., 2015, **119**, 10804.
25. M. I. Muglali, A. Erbe, Y. Chen, C. Barth, P. Koelsch, M. Rohwerder, Electrochim. Acta, 2013, **90**, 17.
26. N. Kemnade, Y. Chen, M. I. Muglali, A. Erbe, Phys. Chem. Chem. Phys., 2014, **16**, 17081.
27. R. J. Nichols, W. Haiss, S. J. Higgins, E. Leary, S. Martin, D. Bethell, Phys. Chem. Chem. Phys., 2010, **12**, 2801.
28. Q. Lu, K. Liu, H. Zhang, Z. Du, X. Wang, F. Wang, ACS Nano, 2009, **3**, 3861.
29. J. M. Beebe, B. Kim, C. D. Frisbie, J. G. Kushmerick, ACS Nano, 2008, **2**, 827.
30. S. H. Choi, B. Kim, C. D. Frisbie, Science, 2008, **320**, 1482.